Retrieval of the Atmospheric Temperature and Humidity Profiles using a Feed-Forward Neural Network †

Raju Pathak[1]*

[1] Centre for Atmospheric Sciences, Indian Institute of Technology Delhi; rajuphyamu@gmail.com
* Correspondence: rajuphyamu@gmail.com; Tel.: +91 9953505418
† Presented at the 4th International Electronic Conference on Atmospheric Sciences, online, July 16-31, 2021.

Abstract: Using a feed-forward neural network, an inverse algorithm was developed to profile the vertical structure of temperature and specific humidity. The inverse algorithm (Inverse model) was used to calculate temperature and humidity profiles, which were then compared with other existing methods. The inverse model is found efficient in profiling the vertical structure of temperature and humidity as compared to other existing methods. For example, the statistical methods notorious for their high computational cost, altitude-dependent error, and inability to retrieve accurately the vertical temperature and humidity profiles, are enhanced with an Inverse model. The inverse model's diurnal and seasonal cycle profiles are also found superior to those of other existing methods, which could be useful for assimilation in numerical weather forecast models. We suggest that incorporating such an Inverse model into the ground-based microwave radiometer (GMWR) will enhance the accuracy of the vertical structure of temperature and humidity profiles, and so the improvement in weather forecasting. The developed inverse model has a resolution of 50 meters between the surface to 500 meters and 100 meters between 500-2000 meters, and 500 meters beyond 2000 meters.

Keywords: Neural Network; Inverse Model; Seasonal and Diurnal Cycle; Radiometer

1. Introduction

The three-dimensional structure of the atmosphere has been widely studied using numerical weather prediction (NWP) models, networks of in-situ radiosonde (RS), and satellite remote sensing [1-4]. Although, RS measurements are prohibitively expensive and biased due to horizontal drifts in the balloon path during high wind conditions [5]. Satellite measurements have been found to overcome these limitations to some extent, but their horizontal and temporal resolution is coarse near to the earth's surface, and so the measured data are not helpful for present-day high-resolution NWP models. Also, Laser radars and Fourier transform infrared spectrometers can profile the atmospheric states, but they do not work in the presence of clouds [6].

In the late twentieth century, researchers reported that a ground-based microwave radiometer (GMWR) can profile the atmospheric temperature, humidity, and cloud liquid water content with high accuracy and perform continuous measurements at an approximate interval of 2-minutes in all weather conditions [7-9]. GMWR measurements have been beneficial in studying several atmospheric processes and improving the predictability of NWP models. For example, over the last two decades, this has been used in severe weather prediction and deriving the diurnal variability of atmospheric stability indices [10], boundary layer studies [11-13], understanding cloud properties [14], and lightening studies [7-8]. In addition, Kadygrov et al. (2013) reported that GMMR is preferable over the other existing methods for studying complex processes such as turbulence fluctuation and changes in heat transfer rate in the atmospheric boundary layer during a solar eclipse.

GMWR uses two built-in functions to profile the vertical structure of atmospheric states. For instance, Function-1 calculates the brightness temperature (radiance) in 20-75 GHz bandwidth using atmospheric water vapor resonance at 22.235 GHz and oxygen resonance at 60 GHz. Function-2 transforms these radiances into atmospheric states. The brightness temperature calculated surrounding the atmospheric water-vapor resonance is preferred for humidity profiling, and the brightness temperature calculated surrounding oxygen resonance is preferred for temperature profiling [16]. The brightness temperature obtained from Function-1 is converted to atmospheric states using an inverse algorithm in Function-2 (also called as Inverse modeling). Such inverse transformation is needed due to the presence of nonlinearity and non-Gaussian caused by the temperature dependence of atmospheric transmission, the Plank function's wave number dependence, clouds, and nonlinear constraints. Inverse techniques used in Function-2 in GMWR to convert the measured brightness temperature from Function-1 to atmospheric states include the Newtonian iteration method (NEM), regression retrieval method (RRM), and neural network method (NNM). NEM performs the mapping of n-dimensional atmospheric state vectors (e.g., temperature, humidity, cloud liquid content, etc.) to the m-dimensional measurement vectors (i.e., brightness temperature; [17]). However, the primary drawback of NEM is the large number of iterations required for an optimal solution and the large error in atmospheric state vectors at higher altitudes. RRM is considered a well-established traditional method in earth and atmospheric science, where atmospheric state vectors are calculated linearly from measurement vectors (i.e., brightness temperature at different frequencies [18-19]), but it produces slightly worst results than NEM due to a linear relationship between dependent and independent vectors. Further, NNM has received global attention by the scientific community to solve the nonlinear problems in atmospheric sciences in the last two decade. For example, Acciani et al. (2003) reported that neural network outperforms other retrieval techniques. Vivekanandan et al. (1997) showed that neural network-based algorithms could incorporate multiple measurements into the retrieval algorithm; however, their application to GMWR (in Function-2) has received lesser attention than other traditional methods.

In this work, we develop an inverse algorithm (Inverse model) using a feed-forward neural network framework to derive the atmospheric temperature and humidity profiles from calculated (and/ or radiometric measured) brightness temperatures at the different frequencies (see Table 1). The paper is structured as below: Section 1 provides introduction, and Section 2 describes the data and Inverse model framework. In Section 2 of the Inverse model framework, the description of a feed-forward neural network, the structure of the Inverse model, and the sensitivity to learning rate are provided. Section 3 presents the results of this work, and Section 4 summarizes the conclusions of this work.

2. Data and Inverse Model Framework

2.1 Data

The daily radiosonde datasets over Mumbai (17.49^o E; 18.57^o N) for 11 years (2006-2016) are used, which are downloaded free from the Upper-Air-Sounding Division of the University of Wyoming (http://weather.uwyo.edu/upperair/sounding.html). The daily radiosonde datasets and existing GMWR brightness temperature over Mahbubnagar, India (78.11^o N; 16.38^o E) during the Cloud-Aerosol Interaction and Precipitation Enhancement (CAIPEX) Integrated Ground Observation Campaign (IGOC) in 2011 is used, which was obtained on request by the Indian Institute of Tropical Meteorology Pune (see https://www.tropmet.res.in/~caipeex/ for more details on CAIPEX data).

We used a total of 825 radiosonde profiles for temperature and 750 radiosonde profiles for humidity in 11-years during January to March, as the remaining profiles were found to have some drastic deformation at higher levels and were therefore excluded from this analysis. The missing data in vertical levels were interpolated using a cubic-spline

interpolation method (as the information of all possible heights was not available). Further, to generate the brightness   77
temperatures at the different frequencies (see Table 1) for 11-year radiosonde observation, a forward model (see Fig. 1   78
and Rambabu et al. 2013 for more details) was used. 70% of the total number of temperature and humidity profiles was   79
used to train the algorithm, while the remaining 30% profiles were used to validate and test the algorithm, each by 15%.   80
In addition, to validate the derived temperature and humidity profile from the developed Inverse model, the existing   81
GMMR data over the Mahbubnagar during the CAIPEX IGOC campaign 2011 was used.   82
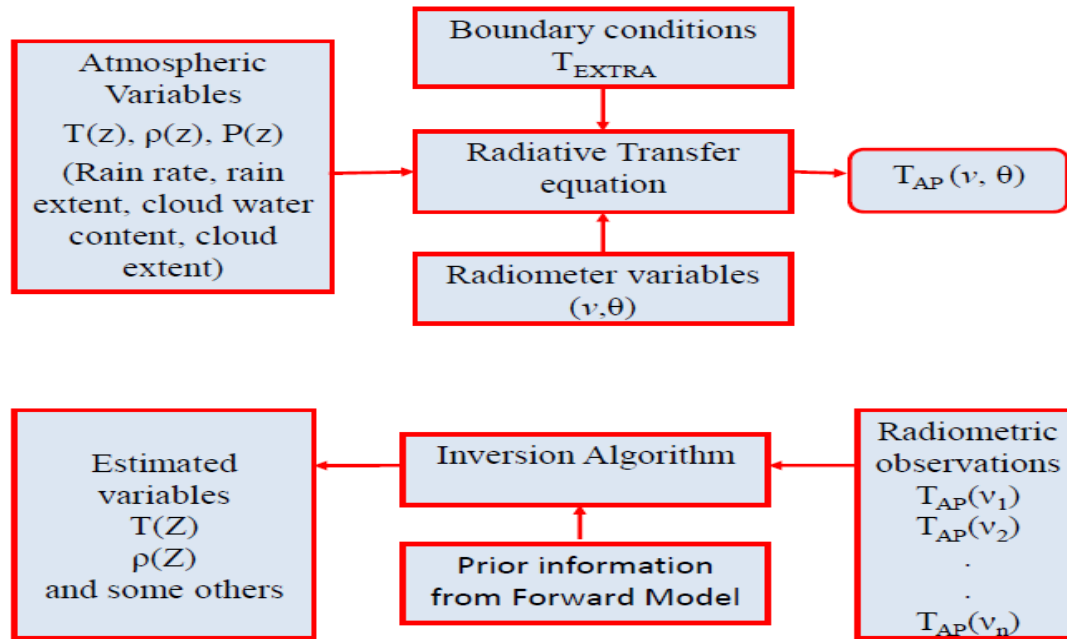
Figure 1: Schematic representation of a forward model (top panel) used to calculate the brightness temperatures at the   83
different frequencies from the atmospheric variables measured by the radiosonde, where the GMWR measured   84
brightness temperature are not available, and the Inverse model (bottom panel) used to calculate the atmospheric   85
variables from the estimated brightness temperature. See Rambabu et al. (2013) for more details on a forward model.   86

Table 1. List of the water vapor and temperature frequency channels used in the ground-based microwave radiometer   87
and in the forward model to estimate the brightness temperature.   88

Sr. no.	Water vapor channel (GHz)	Temperature channel (GHz)
1	22.234	51.248
2	22.500	51.760
3	23.034	52.280
4	23.834	52.804
5	25.000	53.336
6	26.234	53.848
7	28.000	54.400
8	30.000	54.940
9	-	55.500
10	-	56.020
11	-	56.660
12	-	57.288

| 13 | - | 57.964 |
| 14 | - | 58.800 |

2.2 Inverse Model Framework

2.2.1 Feed-Forward Neural Network

A standard feed-forward neural network (FNN) was used for constructing an Inverse model that transforms the forward model calculated (and/ or GMWR radiometric) brightness temperatures at the different frequencies (see Table 1 for list of frequencies) to the atmospheric temperature and humidity profiles. The FNN structure used in this case is composed of three distinct layers: input, hidden, and output (Fig. 2). Additionally, each layer comprises several compute nodes arranged parallelly. All compute nodes in the output layer use a linear function, while all compute nodes in the hidden layer use a nonlinear function (also called an activation function). The activation function specifies a range for the output calculated at hidden nodes, which can be used as input to other hidden layer arranged parallelly or as input to the output layer (see Fig. 2 for more details on FNN structure). The output at a particular hidden node (y), was obtained by weighted-sum of all inputs of the brightness temperature at the different frequencies; see Eq. 1), while the output at a particular node in the output layer (z), is obtained by weighted-sum of all hidden node's output (see Eq. 2).

$$y_j = f\left(\sum_{i=1}^{n} w_{i,j} x_i + b_j \right), \qquad (1)$$

$$x_k = g\left(\sum_{j=1}^{m} w_{j,k} f\left(\sum_{i=1}^{n} w_{i,j} x_i + b_j \right) + c_k \right), \qquad (2)$$

Where x_i is the ith input; $w_{i,j}$ is the associated weight between the ith input node and jth hidden node; $w_{j,k}$ is the associated weight between the jth hidden node and kth output node of the output layer; b and c are the correction factors for hidden and output layers; i, j, and k indices refer to nodes of inputs, hidden, and output layers, respectively. Function $f(\bullet)$ is a nonlinear function (see Eq. 3) and the first derivative of Eq. 3 [i.e., $f'(x) = f(x) - f^2(x)$] is used as a sigmoidal activation function in hidden nodes, and function $g(\bullet)$ is an identity function used in output nodes (see Fig. 2).

$$f(x) = \frac{1}{1 + e^{-x}}, \qquad (3)$$

For the first iteration of FNN, the weights in the hidden and output layers are randomly initialized so that the sum of weights in the hidden layer and the sum of weights in the output layer is less than or equal to 1. The gradient descent back-propagation method is then used to assign these weights to some fixed values. The gradient descent back-propagation method is one of the most straightforward and most efficient method used in supervised learning of a multilayer FNN. The network weights and correction factors in each iteration are updated by propagating errors back to the network (and so-called back-propagation) until the cost function (see Eq. 4) is minimized.

91
92
93
94
95
96
97
98
99
100
101
102
103
104
105
106
107
108
109
110
111
112
113
114
115
116
117
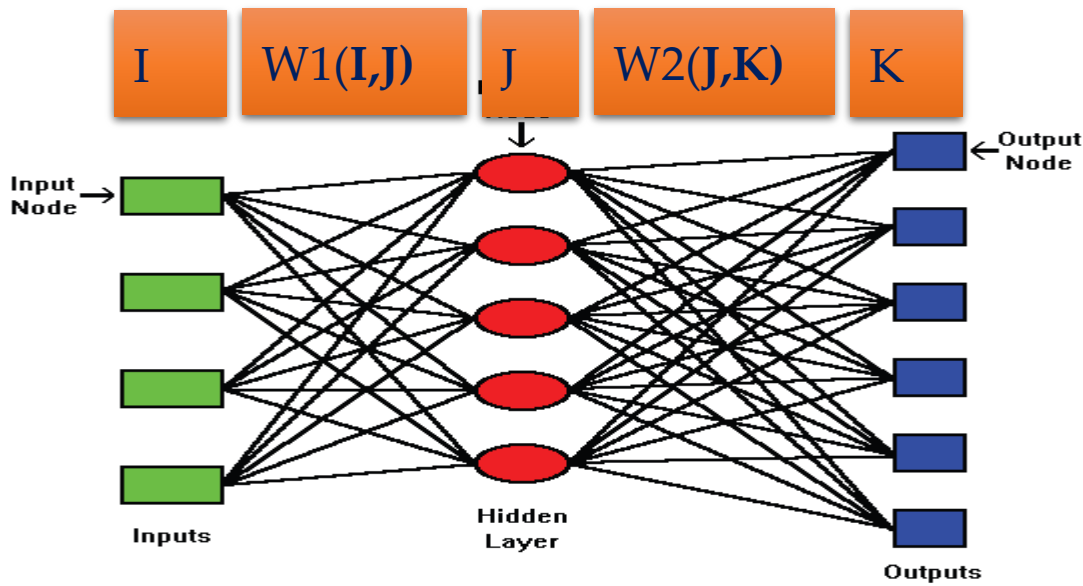
Figure 2: The schematic diagram of a neural network with an example of 5 compute nodes at the hidden layer, 4 input nodes at the input layer and 6 output nodes at the output layer. The weights between the input and hidden layer are given by W1 (i,j), and the weights between the hidden and output layer are given W2 (j,k).

$$J(w) = 1/2 \sum_{k=1}^{c} (t_k - z_k)^2 = \frac{1}{2(t-z)^2},. \qquad (4)$$

$$\Delta W = {}^{\eta}\frac{\partial J}{\partial w}$$

$$\Delta w_{k,j} = {}^{\eta}\delta_k y_j = {}^{\eta}(t_k - z_k) f'(net_k) y_j, \qquad (5)$$

$$\Delta w_{j,i} = {}^{\eta}\delta_j x_i = {}^{\eta}x_i f'(net_j) \sum_{k=1}^{c} w_{kj}\delta_k, \qquad (6)$$

Thus, the weights $w_{i,j}$ in the hidden layer and the weights $w_{j,k}$ in the output layer are updated in each iteration by computing the error δ_k and δ_j at the output and hidden nodes, respectively (see Eq. 5 and Eq. 6). The overall learning (or training) of FNN using Eq. 5 and Eq. 6 for fixing the network weights are controlled by a learning rate (η).

2.2.2 Sensitivity to Learning Rate

To initialize an optimal value of learning rate (η), we performed a sensitivity analysis of η for the estimated value from FNN at the output layer against the number of iterations. The variation of root-mean-square-error (RMSE) against the number of iterations at the three different learning rates (i.e., 0.01, 0.001, and 0.0001) is shown in Figure 3. The RMSE variation against the number of iterations at the other η values between 0.01 and 0.0001 is also calculated but is shown only for the above said η values. The learning rate η specifies the relative size of the weight that needs to be changed during the weight updating process. The RMSE is found to be very sensitive to the learning rate: at a learning rate of $\eta = 0.01$, a large increase in RMSE with an increase in the number of iterations is seen, and at a learning rate of $\eta = 0.001$ and 0.0001, the variation of RMSE against the number of iterations is seen to be optimized. The RMSE, however, is optimized at a slightly lesser number of iterations at $\eta = 0.001$ than at $\eta = 0.0001$. As a result, we use a learning rate of 0.001 for the inverse model in our subsequent analysis of this paper.
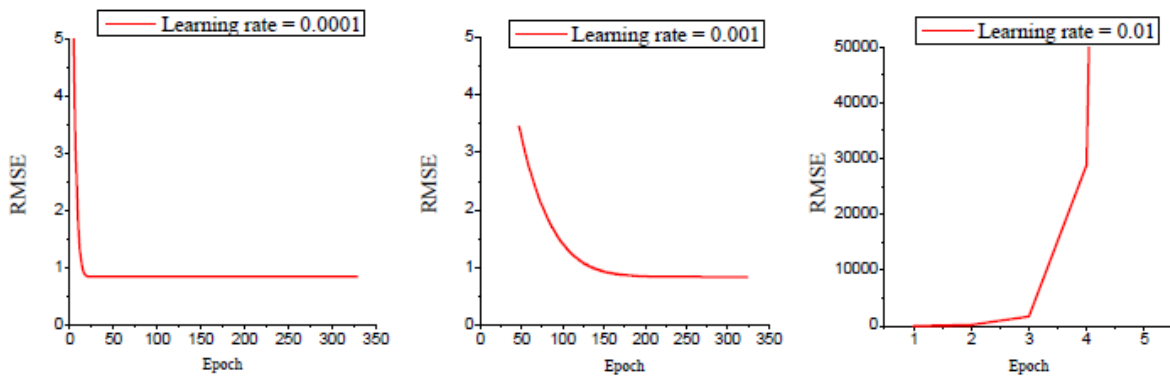
Figure 3: The variation of root-mean-square-error (RMSE) with respect to the variation in the number of iterations (or Epoch) at the different learning rates (e.g., 0.0001, 0.001, and 0.01) for the constructed inverse model.
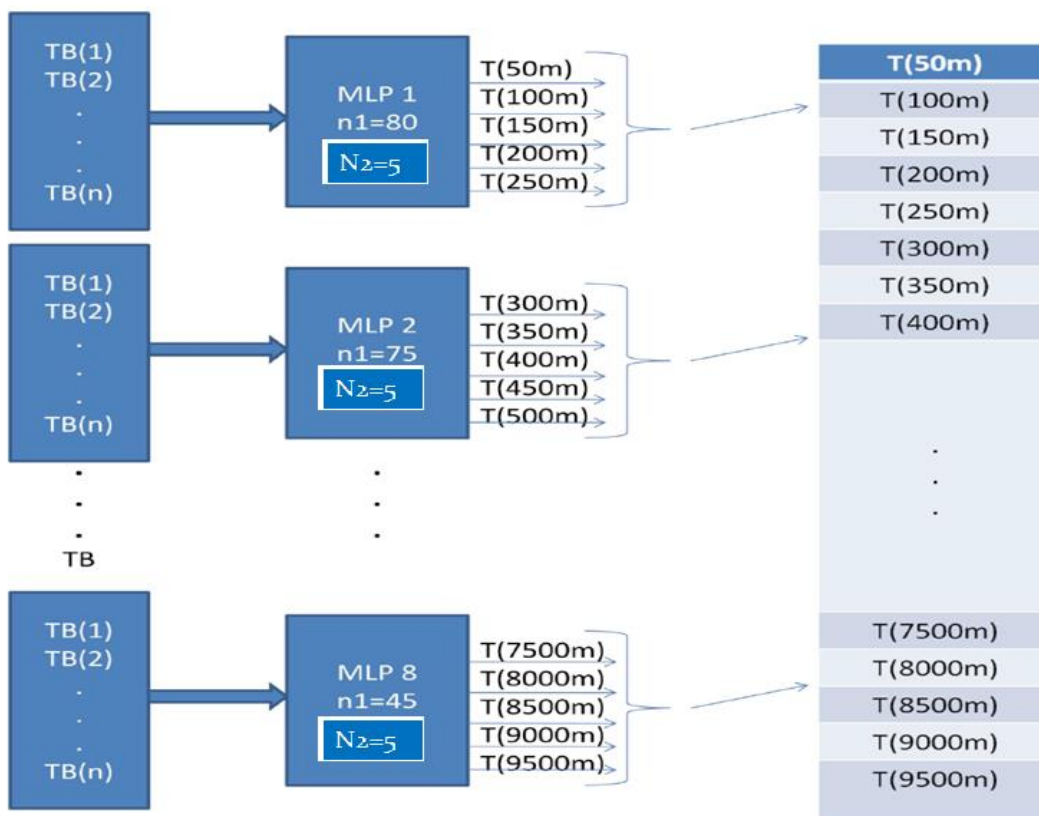
Figure 4: Schematic structure of the Inverse model used to profile the temperature and humidity based on a feed-forward neural network. Here, MLP represents a feed-forward neural network, n1 corresponds to the number of nodes used in the hidden layers, and N2 corresponds to the number of nodes at the output layer. Each MLP structure used in this case can profile temperature and/or humidity at five different heights. A total of 8 MPL completes the inverse model algorithm and profiles the atmospheric variables up to 10 km.

2.2.3 Structure of the Inverse Model

The structure of the proposed FNN to profile temperature and humidity from measured/estimated brightness temperature is shown in Figure 4. We used eight parallel FNN structures arranged in a vertical direction for increasing the accuracy of retrieved vertical profiles. Each FNN is made of five output nodes, with each node corresponding to a different altitude (or height). Thus, we use a total of 40 vertical levels (i.e., 8 FNN * 5 output nodes) with a resolution of 50 m up to 500 m, 100 m between 500 m and 2 km, and 500 m beyond 2 km up to 10 km. The resolutions of vertical levels are divided so that many levels occur close to the earth's surface. Most of the other existing methods are deteriorate/coarser to examine the processes occurring closure to the earth's surface. In addition, we also use a large number of hidden nodes in the FNN structure that are close to the earth's surface (see Fig. 4). Therefore, the complete FNN framework is used as an inverse model to estimate the temperature and humidity value at the various vertical levels.

3. Results

Figures 5, and 6 show vertical profile of temperature and humidity, respectively, from Inverse model and radiosonde (RS) observation over Mumbai on three different days during winter season (December to February; or DJF). The brightness temperature at different frequencies (see Table 1) over Mumbai (an input to Inverse model) is calculated using forward model because radiometric brightness temperature estimated from GMWR was not availbable (see Rambabu et al. 2013 for more details on forward model and GMWR measurement).
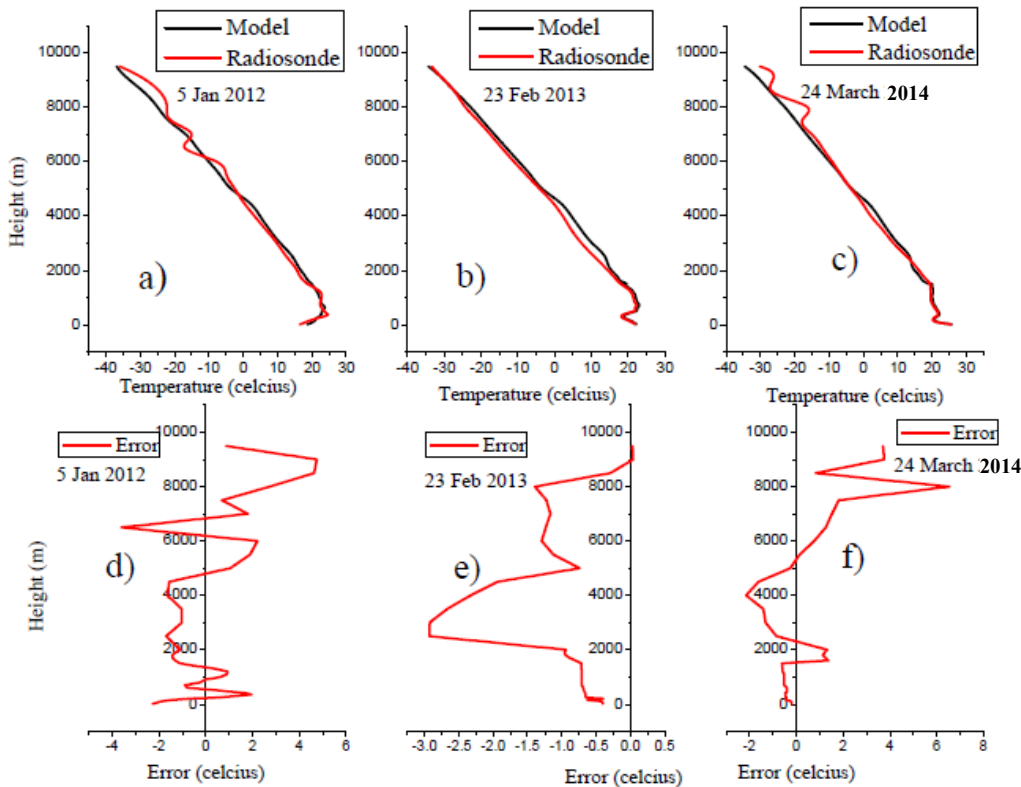
Figure 5: Vertical temperature profile for three different days over Mumbai: **a)** 5th January 2012, **b)** 23rd February 2013, and **c)** 24th March 2014, from an inverse model (in black) and radiosonde observation (in red), as well as the corresponding differences **(d - f)**. The brightness temperatures that are fed as an input to the Inverse model, are calculated from a forward model using radiosonde observation.

The vertical profile of temperature and humidity calculated from the Inverse model varies very similarly to that obtained from the RS observation on all three days. The Inverse model based on a feed-forward neural network well captures the temperature inversion seen in the RS observation. The temperature inversion occurs when a layer of cool air at the surface is overlain by a layer of warmer air, causing a reversal in temperature structure within the boundary layer (i.e., air temperature increases despite decreasing with an increase in height). Further, in both the RS observation and the inverse model, the maximum variation of humidity is seen near the earth's surface (Fig. 6). This maximum variation in humidity profile close to the earth's surface is most likely due to precipitation, dew, and fog. Furthermore, if we consider the temperature and humidity vertical profiles obtained from RS observation as true profiles, we find that Inverse model overestimated/or underestimated (at some levels) by about ±2 °C for temperature, ±4 g/kg for humidity in the lower troposphere, and about +4 °C for temperature and ±0.1 g/kg for humidity in the upper troposphere for all three successive days, as compared to RS observation. However, these overestimation and underestimation in the vertical profile of temperature and humidity can not be considered to be 100% accurate as the RS observation can itself have some measurement bias due to the drift in baloon path during high horizontal wind flow and in fog or rain conditions).
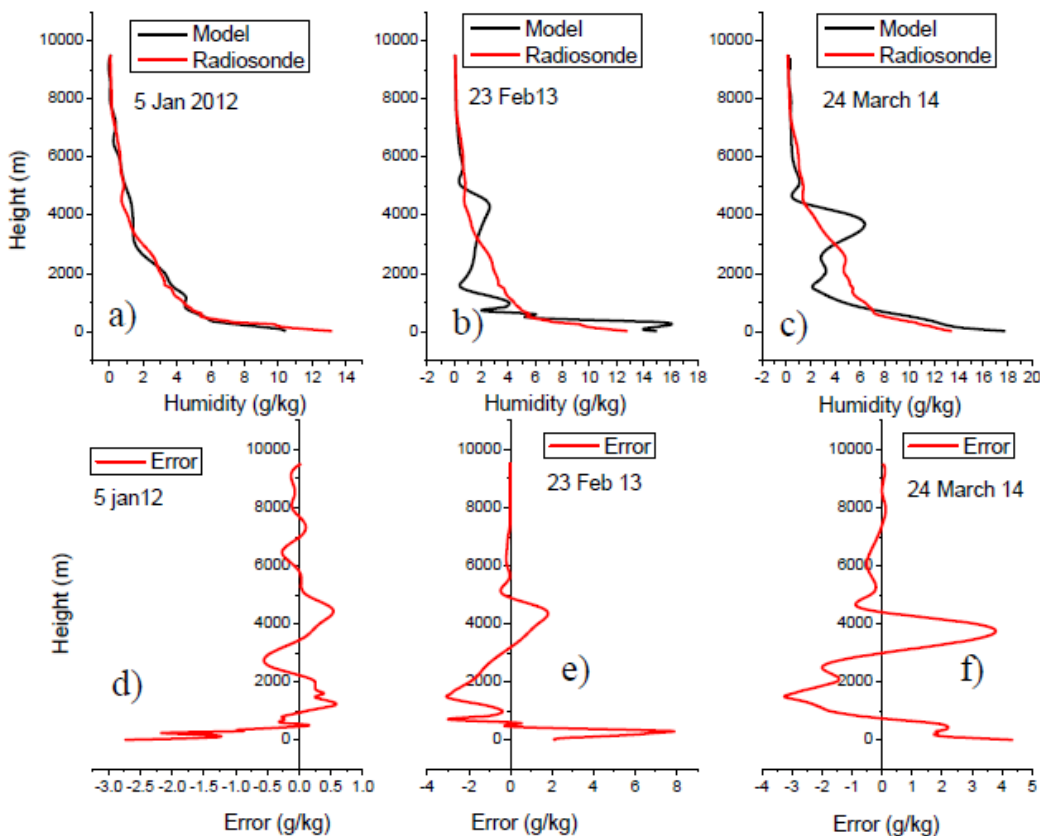
Figure 6: Same as Figure 5 but for specific humidity profile.

In addition to validating Inverse model's result with RS observation, we also validate Inverse model with an existing GMWR along with RS observation for two different days over Mahbubnagar, India, during the CAIPEX IGOC campaign in 2011, using Figures 7, and 8 for temperature and humidity, respectively. In this case, the brightness temperature measured by an existing GMWR over Mahbubnagar is used as an input to Inverse model instead of calculating it from RS observation using the forward model. We find good agreement between existing GMWR, RS, and

Inverse model in the lower troposphere. The large difference in vertical temperature and humidity profile   188
overestimation/ or underestimation seen between RS observation and GMWR is seen to be reduced between the RS   189
observation and inverse model. For example, the temperature profile calculated from Inverse model shows a much   190
smaller overestimation/or underestimation than that seen in existing GMWR with respect to RS observations at all levels.   191
The profiles calculated from Inverse model agree well with RS observation than the existing GMWR, not only for   192
temperature but also for humidity, as evidenced by the reduced bias at all heights compared to the existing GMWR.   193
Further, we investigate how the inverse model estimates the diurnal cycle of humidity and temperature with respect to   194
existing GMWR during the CAIPEX IGOC 2011 over Mahbubnagar for three successive days from 29 to 31st October   195
2011. Figure 9 shows the time-height plots of temperature and humidity from the inverse model and existing GMWR   196
and their corresponding differences. In addition, we find that the temperature and humidity profiles retrieved from an   197
existing GMWR and inverse model are close at all levels except minor irregularities near the surface. The difference   198
between the existing GMWR and inverse model is noted in the range of (+3, -1) ^{o}C for temperature, ±1 g/kg for humidity   199
in the lower troposphere, and in range of (+1.5, -4) ^{o}C for temperature and minimal difference for humidity in the upper   200
troposphere. The temperature inversion can be seen in diurnal variation as well with both methods.   201
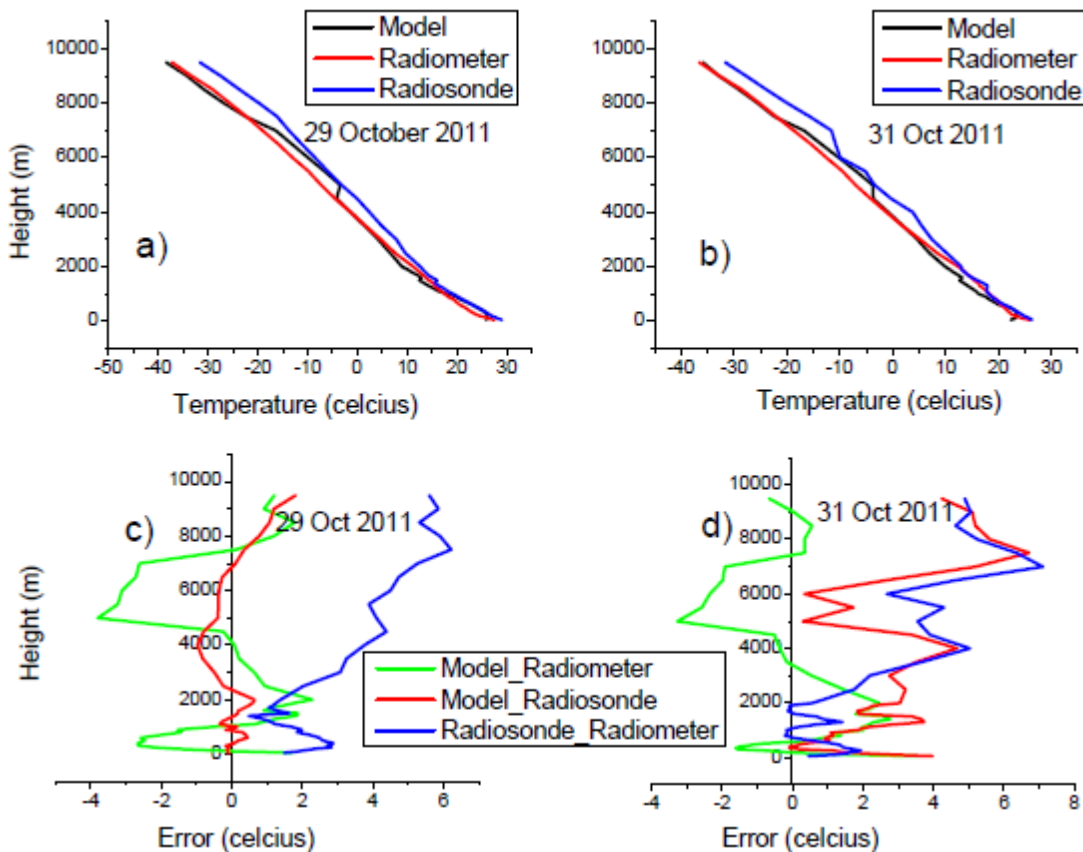
Figure 7: Vertical temperature profile over the Mahbubnagar during the CAIPEX IGOC campaign on **a)** 29th October   202
2011 and **b)** 31st October 2011 for three different retrieval techniques (i.e., Inverse model, existing ground-based   203
microwave radiometer, and the radiosonde observation), as well as the corresponding **(c and d)**   difference. The   204
brightness temperatures that are fed to as an input to Inverse model are taken from the existing ground-based   205
microwave radiometer.   206
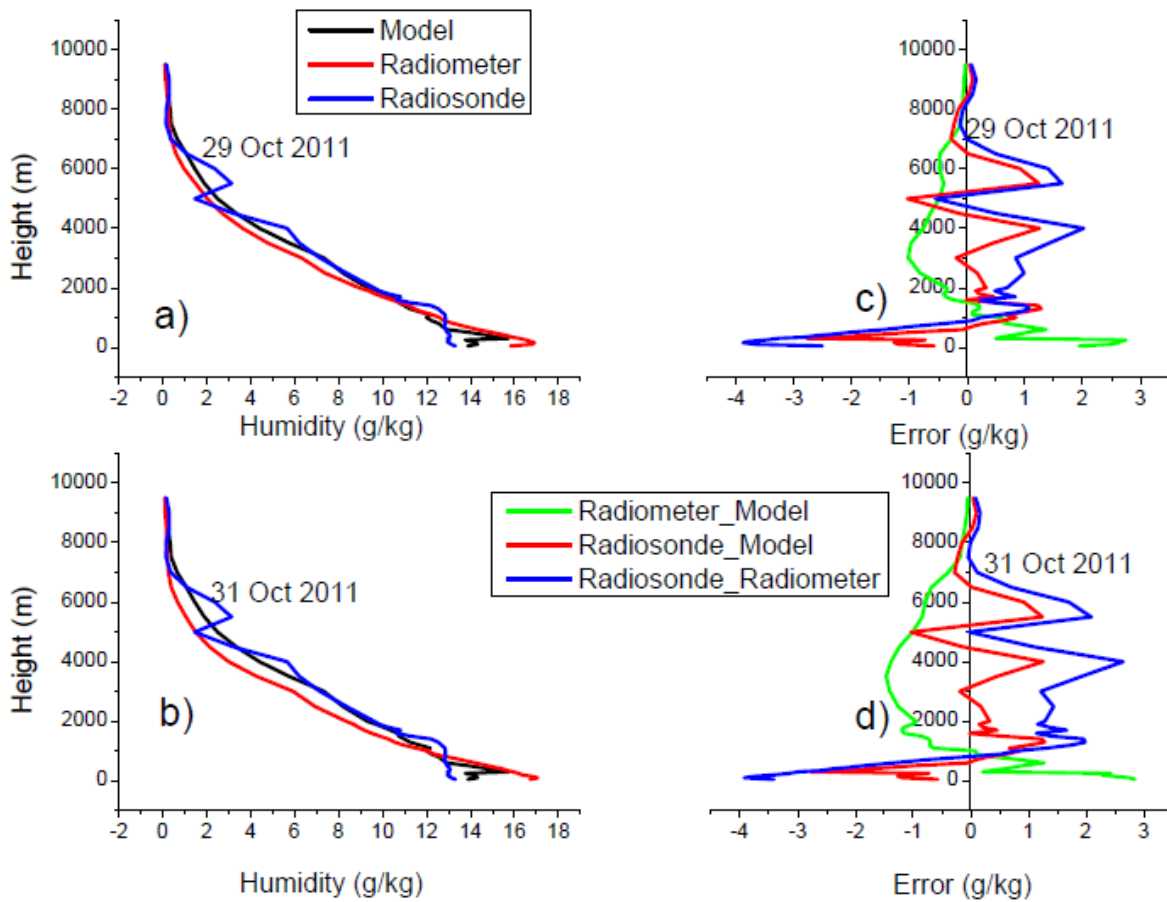
Figure 8: Same as Figure 7 but for specific humidity.

Furthermore, Figure 10 shows daily annual variation of temperature and humidity vertical profiles over Mumbai from Inverse model and RS observation during 2014, with an input of brightness temperature to Inverse model computed using a forward model from RS observation. The difference in temperature and humidity profiles between the inverse model and RS observation are also shown in Figure 10 (e and f). The rapid fall in temperature and increase in humidity during the transition of pre-monsoon to monsoon period and the increase in temperature and decrease in humidity during the transition of monsoon to the post-monsoon period seen in RS observation are well captured in magnitude and pattern by Inverse model. In both the RS observation and Inverse model, we find a stable humidity variation during winter, and the maximum variation of temperature and humidity is located near the earth's surface regardless of seasons. From the difference between the inverse model and RS observation, we find the difference in range of (-1 to -4) ^{o}C below 1.5 Km, 2 to 4 ^{o}C above 7 Km, and ±1 ^{o}C for the rest of the heights for temperature during the monsoon period. However, in the case of humidity, we notice the large differences during the monsoon periods and lesser difference during the rest of the periods, with a variation of ±1.5 g/kg for all heights in all seasons except during the monsoon season where it is about 3 to 5 g/kg.
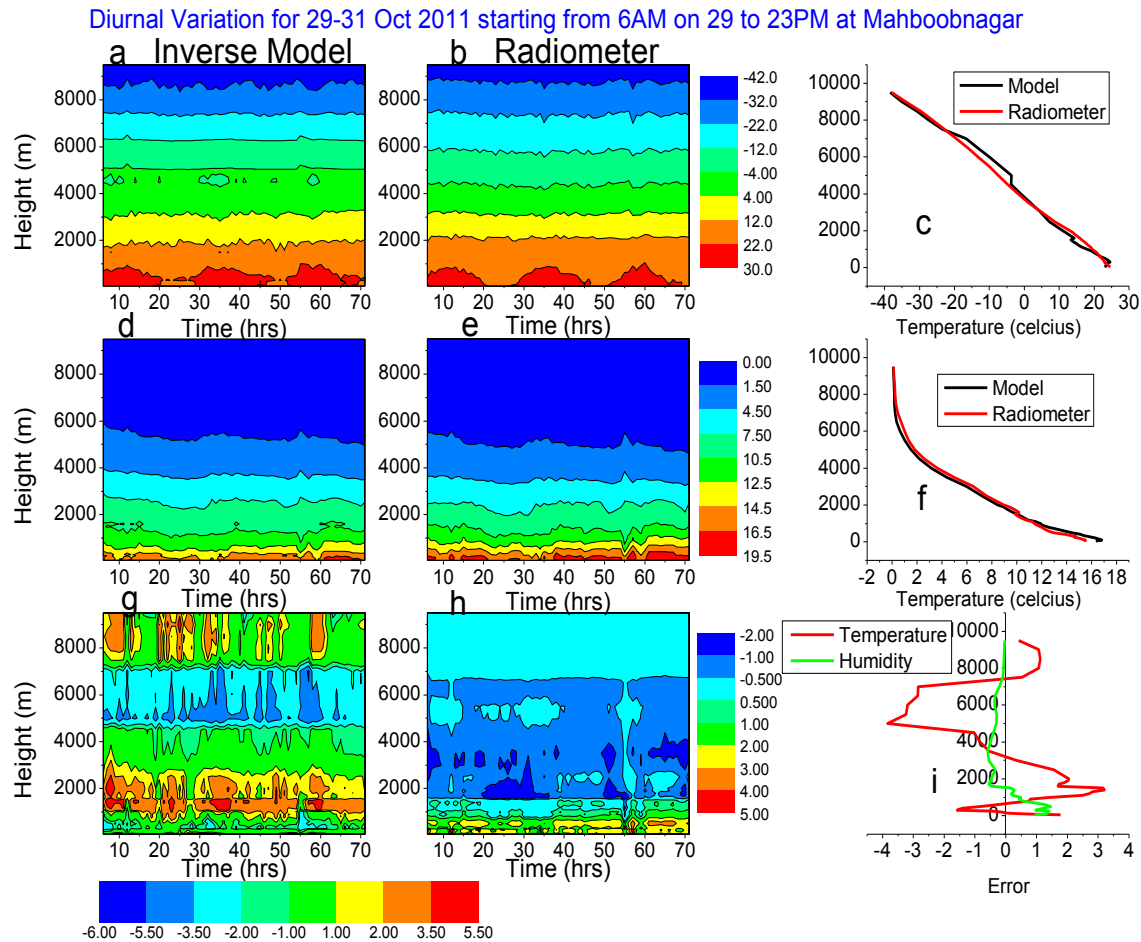
Figure 9: Time-height plot for the diurnal variation of temperature **(a, b)** and specific humidity **(d, e)** over Mahbubnagar during the 29-31st October 2011 in CAIPEX IGOC campaign from the ground-based microwave radiometer (GMWR) and the inverse model, as well as the difference plot for temperature **(g)** and humidity **(h)**. Right panels **(c, f, and i)** of the figure show the 3-day mean profile of temperature **(c)** and humidity **(f)**, and the corresponding difference (error) plot **(i)** for temperature and humidity between the GMWR and the inverse model.

4. Conclusions

An inverse algorithm (Inverse model) was developed to profile the vertical structure of temperature and humidity in the troposphere, using a feed-forward neural network. Inverse model has been used to calculate several temperatures and humidity profiles and compared with different existing techniques/methods. The inverse model is found more efficient in profiling the temperature and humidity vertical structure than other existing methods. The statistical methods used in the existing ground-based microwave radiometer (GMWR), known for their high computational cost and altitude-dependent inaccuracy, and inability to estimate the vertical temperature and humidity profile, are enhanced when an Inverse model is used. The diurnal and seasonal cycle of temperature and humidity vertical profiles calculated by Inverse model outperformed other existing methods, which could be helpful for assimilation in numerical weather prediction models. We suggest that introducing such an Inverse model into GMWR will improve/increase the accuracy of temperature and humidity retrieval and so the improvement in weather forecasting.

Comparision of model retrieved seasonal variation with radiosonde observation over Bombay for 2014

On X - Axis; Time (in Days number) while the different color coding have degree celcius and g/kg unit for emperature and humidity respectively. Horizontal Color line is error scale for temperature
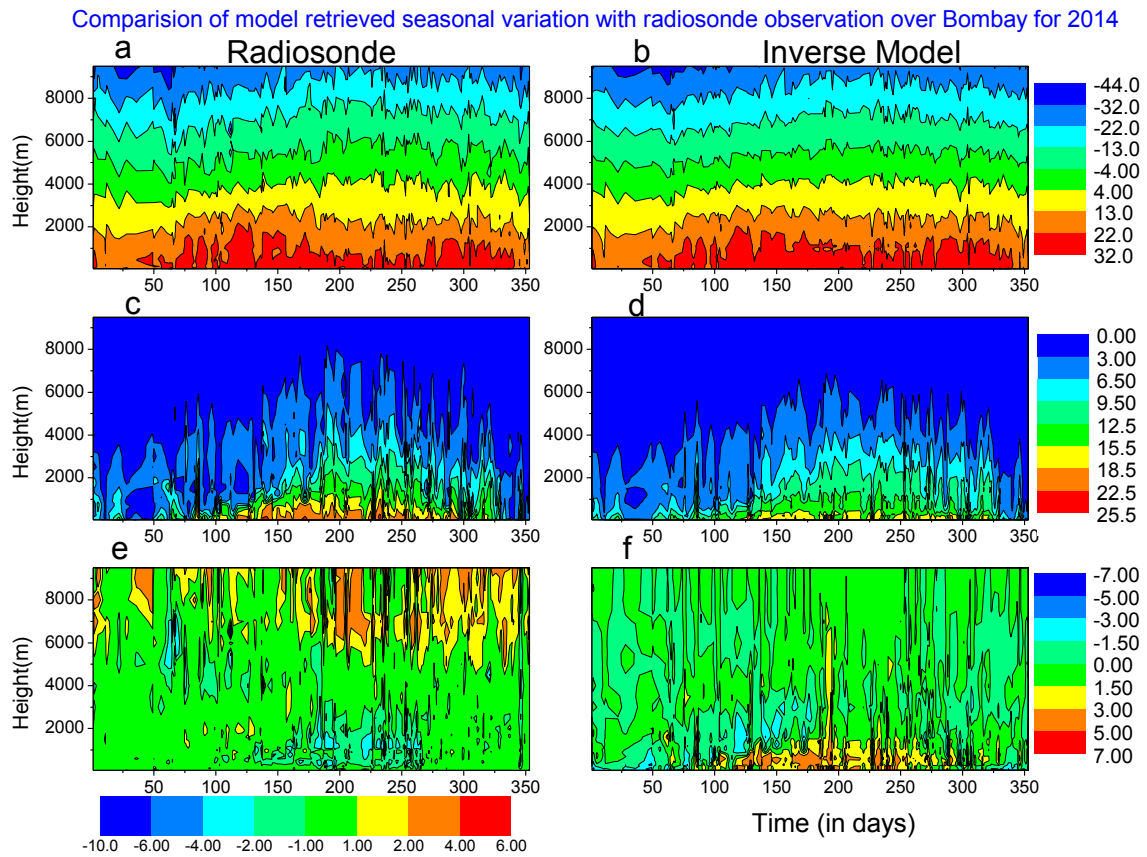
Figure 10: Time-height plot for the annual variation of temperature (degree Celcius; **a, b**) and specific humidity (g/kg; **c, d**) over Mumbai during 2014 from the radiosonde observation **(a, c)** and the inverse model **(b, d)**, as well as the difference plot for temperature **(e)** and humidity **(f)** between the inverse model and the radiosonde observation.

References

1. Barrett, E.C., Hamilton, M.G. Potentialities and problems of satellite remote sensing with special reference to arid and semiarid regions. *Climatic Change*, 1986, 9, 167–186. https://doi.org/10.1007/BF00140534

2. Trenberth, K. E. The use and abuse of climate models. *Nature*, 1997, 386 (6621) 131–133. doi:10.1038/386131a0.

3. Rodwell, M.J., Palmer, T.N. Using numerical weather prediction to assess climate models. *Q J R Meteorol Soc*, 2007, 133, 129–146. https://doi.org/10.1002/qj.23

4. Yang, J., Gong, P., Fu, R. et al. The role of satellite remote sensing in climate change studies. *Nature Clim Change, 2013,* 3, 875–883. https://doi.org/10.1038/nclimate1908

5. Luers, J.K, Eskridge, R.E. Use of radiosonde temperature data in climate studies. *J. Climate*, 1998, 11, 1002–1019

6. Karmakar, P. Ground-based microwave radiometry and remote sensing: Methods and applications. *Boca Raton, CRC Press., 2013,* 214, ISBN 978146651631.

7. Decker, M.T., Westwater, E.R., and Guiraud., FOF.O. Experimental evaluation of ground-based microwave radiometric sensing of atmospheric temperature and water vapor profiles. *J. Appl. Meteorol.*, 1978, 17, 1788-1795.

8. Askne, J., and Westwater, E. A review of ground-based remote sensing of temperature and moisture by passive microwave radiometers. *IEEE Trans. Geosci. Remote sens.*, 1986, GE-24, 340-352.

9. Acciani, G. Orazio, A.D. Radiometric profiling of temperature using algorithm based on neural network. *IEEE electronics letters*, 2003, 39(17).

10. Madhulatha, A., Rajeevan, M. Nowcasting severe convective activity over southeast India using ground-based microwave radiometer observations. *Journal of Geophysical Research: Atmosphere*, 2013, 118, 1–13. doi:10.1029/2012JD018174, 2013

11. Crewell, S., Czekala, H., Lohnert, U., Simmer, C., Rose, T., Zimmermann, R. and Zimmermann, R. Microwave radiometer for cloud carthography: A 22-channel ground-based microwave radiometer for atmospheric research. *Radio Science*, 2001, 36, 4, 621-638.

12. Szalowski, K. The effect of the solar eclipse on the air temperature near the ground. *J. Atmos. Solar Terrestr. Phys.*, 2003, 64(15), 1589–1600

13. Cimini, D., Rizi, V., Di Girolamo, P., Marzano, F.S., Macke, A., Pappalardo, G., Richter, A. Overview: tropospheric profiling: state of the art and future challenges – introduction to the AMT special issue. *Atmos. Meas. Tech., 2014, 7*, 2981–2986. https://doi.org/10.5194/amt-7-2981-2014

14. Harikishan, G., Padmakumari, B., Maheskumar, R.S., Pandithurai, G. Macrophysical and microphysical properties of monsoon clouds over a rain shadow region in India from ground-based radiometric measurements. *Journal of Geophysical Research*, 2013, 10.1002/2013JD020872

15. Kadygrov, E.N. Study of Atmospheric Boundary Layer Thermodynamics During Total Solar Eclipses. *IEEE Transactions on Geoscience and Remote Sensing*, 2013, 51 (9).

16. Solheim F, Godwin, J., Westwater, E.R., Han, Y., Keihm, S., Marsh, K., and Ware., R. Radiometric profiling of temperature, water vapor and cloud liquid water using various inversion methods. *Radio Sci.*, 1998, 33, 393-404.

17. Han, Y., and Westwater, E.R. Remote sensing of tropospheric water vapor and cloud liquid water by integrated ground-based sensors. J. Atmos. Oceanic Technol., 1995, 12, 1050–1059.

18. Westwater, E. R. Ground-based microwave remote sensing of meteorological variables. *Atmospheric Remote Sensing by Microwave Radiometry.* M. A. Janssen, Ed., J. Wiley and Sons, Inc., 1993, 145–213.

19. Rodgers, C.D. Retrieval of Atmospheric Temperature and Composition from Remote Measurements of Thermal Radiation. *Reviews of geophysics and space physics*, 1976, 14(4).

20. Acciani, G., Orazio, A.D. Radiometric profiling of temperature using algorithm based on neural network. *IEEE electronics letters*, 2003, 39(17)

21. Vevekanandan, J. Development of neural network - based inversion method part-1. *IEEE publication*, 1997, 35(2).

22. Rambabu, S. Pillai, J.S., Agarwal A., and Pandithurai, G. Evaluation of brightness temperature from a forward model of ground-based microwave radiometer. *J. Earth Syst. Sci.*, 2014, 123(4), 641–650.